PCCP

View Online
Dynamic Article Links

Cite this: *Phys. Chem. Chem. Phys.*, 2011, **13**, 5855–5871

www.rsc.org/pccp

PAPER

Monomer, clusters, liquid: an integrated spectroscopic study of methanol condensation†

Hartawan Laksmono,‡[a] Shinobu Tanimura,[a] Heather C. Allen,[b] Gerald Wilemski,[c] Mark S. Zahniser,[d] Joanne H. Shorter,[d] David D. Nelson,[d] J. Barry McManus[d] and Barbara E. Wyslouzil*[ab]

Received 10th November 2010, Accepted 14th January 2011
DOI: 10.1039/c0cp02485f

We have combined static pressure, spectroscopic temperature, Fourier transform infrared spectroscopy (FTIR), and small angle X-ray scattering (SAXS) measurements to develop a detailed picture of methanol condensing from a dilute vapor–carrier gas mixture under the highly supersaturated conditions present in a supersonic nozzle. In our experiments, methanol condensation can be divided into three stages as the gas mixture expands in the nozzle. In the first stage, as the temperature decreases rapidly, small methanol *n*-mers (clusters) form, increase in concentration, and evolve in size. In the second stage, the temperature decreases more slowly, and the *n*-mer concentrations continue to rise. Thermodynamic and FTIR experiments cannot, however, definitively establish if the average cluster size is constant or if it continues to increase. Finally, when the vapor becomes supersaturated enough, liquid droplets form *via* nucleation and growth, consuming more monomer and reducing the concentration of clusters. At the point where liquid first appears, cluster formation has already consumed up to 30% of the monomer. This is significantly more than is predicted by a model that describes the vapor phase as an equilibrium mixture of methanol monomer, dimer, and tetramer. An energy balance suggests that a significant fraction of the cluster population is larger than the tetramer, while preliminary SAXS measurements suggest that these clusters contain, on average, 6 monomers.

I. Introduction

The formation of clusters (*n*-mers) in the vapor phase of methanol (MeOH), attributed to hydrogen bond formation, has long been investigated using a wide variety of experimental and computational approaches. Although the exact distribution and the properties of these *n*-mers are still not established, the physical and transport properties of methanol vapor can only be understood by invoking their presence.[1–11] Equilibrium constants derived by fitting thermal conductivity[6–8] and heat capacity[3] measurements above room temperature suggest that the vapor phase consists primarily of monomers, dimers, and tetramers, while a vapor phase comprising monomers, trimers, and octamers provides a better fit for vapor pressure measurements near room temperature.[11] Complementary low temperature infrared (IR) spectroscopy experiments,[12,13] where rotational temperatures are as low as ~5 K, are able to observe distinct peaks for the monomer through tetramer. More complex experiments have measured the IR absorption spectra of size selected clusters containing up to 9 methanol molecules for temperatures T ranging from 93 K to 135 K.[14–18] Even at room temperature, absorption features due to dimers and tetramers can be observed in the OH stretch region[13] although these do not have the sharp peaks seen in the low T data. Furthermore, the absorption peaks at low temperature are shifted by 30–100 cm^{-1} to lower wavenumbers relative to those observed in the room temperature spectra. Low temperature IR absorption studies have also been able to distinguish different structural conformations. In the cyclic methanol hexamer cluster, for example, Steinbach *et al.*[16] observed the transition from the chair isomer to the boat isomer with increasing temperature. However, interpreting the finer structural details of the OH stretch region of the low temperature IR spectra is not trivial and requires additional techniques. For example, a combined IR and Raman spectroscopy study demonstrated that the spectral complexity in the low

[a] *William G. Lowrie Department of Chemical and Biomolecular Engineering, The Ohio State University, Columbus, OH 43210, USA. E-mail: wyslouzil.1@osu.edu*
[b] *Department of Chemistry, The Ohio State University, Columbus, OH 43210, USA*
[c] *Department of Physics, Missouri University of Science and Technology, Rolla, MO 65409, USA*
[d] *Center for Atmospheric and Environmental Chemistry, Aerodyne Research Inc., Billerica, MA 01821, USA*
† Electronic supplementary information (ESI) available. See DOI: 10.1039/c0cp02485f
‡ Current address: Stanford PULSE Institute for Ultrafast Energy Science, SLAC National Accelerator Laboratory, 2575 Sand Hill Rd MS59, Menlo Park, CA 94025, USA

temperature OH stretch region of the trimer and tetramer corresponds to the umbrella motions of the associated methyl group rather than structural isomers.[19,20] Recently, other techniques such as X-ray photoelectron spectroscopy experiments have been used to observe small clusters produced by adiabatic expansion.[21] In their experiments (T not reported), Bergersen *et al.*[21] observed spectra that were consistent with two size regimes of clusters; small cyclic oligomers that they estimated to range from trimer to octamer, and medium sized clusters containing hundreds of molecules. Surprisingly, there was little evidence for the presence of dimers.

Theoretical calculations both complement the experimental work and help interpret the complex spectra. Quantum mechanical computational studies of methanol clusters[22–24] have been conducted for clusters up to $n = 20$, depending on the level of theory and accuracy used, while Monte Carlo methods were employed for clusters[25,26] containing up to $n = 256$ molecules. These studies find that the stability of the small clusters increases with increasing number of molecules in the clusters, and once the clusters contain 5 to 6 molecules, cluster energy per molecule converges to an asymptotic value.[23,24] Clusters in which the methanol molecules form closed ring structures are also more stable than those that adopt chain configurations.[22–24] Calculations that include multiple structural configurations per cluster size show that once clusters contain 5–6 molecules the average OH stretching frequency has decreased from that of the vapor, $\sim$3680 cm^{-1}, to that of the liquid, $\sim$3337 cm^{-1}.[23,27] In addition to the change in frequency, the OH stretching band for liquid methanol is both broader and has less structure than equivalent bands for the monomers or isolated low temperature clusters in the vapor phase. Nevertheless, in experiments near room temperature, Ohno *et al.*[28] analyzed the broad OH absorption feature of the liquid and assigned contributions to the intensity at different wavenumbers to hydrogen bonding environments that originate from cluster configurations in the liquid with $n = 2$–7.

In addition to providing insight into the phenomenon of hydrogen bonding, associated vapor phase molecules are of interest because they bridge the gap between the monomer and the condensed phase. In the simplest view of the vapor-to-liquid phase transition, monomers in a supersaturated vapor combine to form dimers, trimers, tetramers, and so on until clusters large enough to be in unstable equilibrium with the supersaturated vapor—the critical clusters—rapidly grow to macroscopic size, depleting the mother phase and pushing the system toward equilibrium. For most species commonly studied by the nucleation community, the formation of clusters smaller than the critical size does not appreciably change the monomer concentration or perturb the experiments in any other way. Thus, characterizing the temperature, vapor phase concentration, and supersaturation corresponding to the nucleation conditions is reasonably straightforward, as is the comparison of measured rates with theoretical predictions. In our work,[29–31] we use supersonic nozzles to investigate homogeneous nucleation and growth of droplets from the supersaturated vapor phase. For methanol, vapor phase association may play a critical role in condensation. This paper describes our efforts to follow the phase transition of methanol in detail, and to determine whether, as was assumed by others,[32,33] the vapor is adequately described by a monomer–dimer–tetramer equilibrium model prior to the appearance of the liquid. With our highly instrumented experimental apparatus we can independently measure the pressure and temperature of the flowing gas mixture using a static pressure probe and tunable diode laser absorption spectroscopy (TDLAS), respectively, characterize the droplets using small angle X-ray scattering (SAXS), and follow the depletion of the methanol vapor and the appearance of hydrogen-bonded methanol species using Fourier transform infrared spectroscopy (FTIR). By making position resolved measurements we are able to follow changes in the distribution of methanol between the vapor, small clusters and the liquid state with microsecond resolution. Combining these independent techniques, we develop a more complete picture of methanol condensation as well as test the adequacy of existing models to describe the distribution of methanol among the different species.

II. Experimental methods and analysis

In this section, we describe the basic phenomenon of condensation in a supersonic flow and outline the analytical approach that will let us characterize the properties of the flow from the measured variables. We then present the flow system and supersonic nozzles used to generate methanol vapor clusters and liquid droplets followed by a discussion on each measurement technique.

A Supersonic flow with condensation

A supersonic flow of a dilute condensible vapor–carrier gas mixture in a gently expanding Laval nozzle can be considered adiabatic because, in most cases, heat transfer from the surroundings and energy losses due to friction are negligible. As the gas mixture expands in the nozzle, there is a rapid decrease in pressure, temperature, and density, and an increase in velocity. If the temperature is low enough, the vapor can become supersaturated and initiate a phase transition. The heat released by the phase transition to the surrounding gas increases the pressure, temperature, and density and decreases the velocity relative to that expected for the continued isentropic expansion of the gas mixture. The decrease in supersaturation, due to the increase in temperature and depletion of the monomer, quenches nucleation while droplet growth continues to deplete the monomer, add energy to the flow, and push the system toward equilibrium.

Adiabatic supersonic flow with condensation can be described by considering an equation of state for the gas mixture together with the conservation laws for mass, momentum, and energy. If the expansion is gentle, as in our case, the flow in the Laval nozzle can be assumed to be one dimensional, resulting in four governing equations that relate the following six variables—static pressure p, temperature T, density of the fluid (including any condensate) ρ, velocity u, effective area ratio A/A^*, where A^* is the minimum cross sectional area in the nozzle, at the nozzle throat, and mass fraction of condensate g. Thus, by measuring two variables as a function of axial position in the nozzle, the remaining variables can be determined by solving the position dependent equations.[34,35]

In the standard formulation of the adiabatic supersonic flow equations, the equation of state for the vapor carrier gas mixture neglects the contribution from *n*-mers because, for most vapors, the concentration of dimers, trimers, tetramers, *etc*. is so much lower than that of the monomer and their molecular weights are higher. Likewise, any heat release to the flow is assumed to be due to the formation of a bulk liquid rather than by the formation of low *n* clusters *via* vapor phase association. For many substances, including, for example, D_2O,[35] these assumptions are entirely adequate.

For methanol condensation in a supersonic nozzle, the temperatures are low, the supersaturations are high and, based on simple equilibrium calculations, we expect significant vapor phase association to occur. To account for this phenomenon, we incorporate the effect of clustering into the flow equations following the approach developed by Tanimura *et al.*[36] In particular, we modify the equation of state to explicitly include clusters, incorporate an equilibrium model to estimate the concentration of the *n*-mers as a function of temperature and methanol vapor concentration, and estimate the heat release to the flow by the formation of clusters. Any additional heat release to the flow is assumed to stem from the formation of liquid. The final equations describing the flow in the nozzle for a vapor–carrier gas mixture containing one condensible species are presented in the appendix.

The easiest variable to measure is the static pressure distribution. If we use the static pressure of the non-condensing flow to determine the effective area ratio of the expansion, *i.e.* the area ratio that includes the growth of boundary layers along the nozzle surfaces, and, furthermore, assume that the boundary layers are unaffected by the condensation processes, we can solve the supersonic flow equations using the area ratio and static pressure as input. Unfortunately, under our experimental conditions, the boundary layers are slightly compressed by the condensation process and, consequently, the temperature and mass fraction condensate are noticeably underestimated,[35] while velocity and density are less affected. A more accurate approach is to use the average temperature of the condensing flow—measured using TDLAS as described in Section IID—and the static pressure as the measured inputs. If we further assume that the boundary layer is laminar in the region of decreasing pressure, this approach makes it possible to directly account for compression of the boundary layer during condensation and improves the accuracy of the estimates for the other variables, in particular the centerline temperature of the flowing gas mixture.[36]

B Flow apparatus and supersonic nozzles

We performed the experiments using the same flow apparatus, illustrated in Fig. 1, that was used in our previous TDLAS[36–38] and SAXS[30,31,39] experiments. Briefly, ~18 mol min^{-1} N_2 carrier gas, drawn from the gas side of two liquid nitrogen Dewars, is warmed to room temperature using 1000 W inline heaters. Pressure regulators control the pressure at the entrance of the mass flow controllers. One of the gas streams enters the vapor generator where part of the flow disperses the methanol liquid into droplets while the remainder provides additional energy to evaporate the drops and further dilute the vapor mixture. The methanol liquid is introduced to the vapor generator by pumping the liquid from a flask using a peristaltic pump. We measure the methanol liquid flow rate by monitoring the weight change of the flask using a balance. The vapor rich gas mixture is combined with the remaining carrier gas and a pure methane stream (0.333 mol min^{-1}) using a third mass flow controller. The methane does not condense but, as detailed in Section IID, is used in the TDLAS experiments to measure the average temperature of the flow. The mass flow

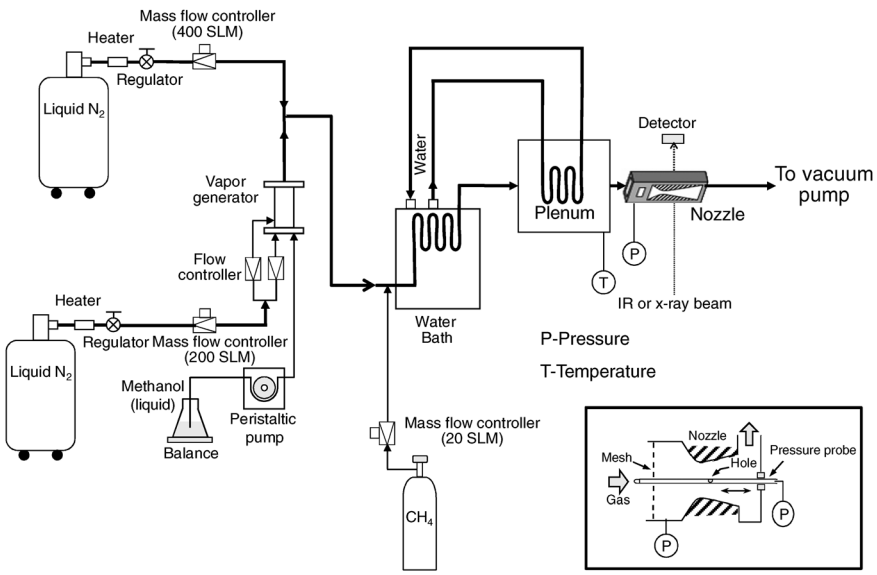

Fig. 1 A schematic diagram of the experimental setup used to conduct the pressure trace measurements (PTM), tunable diode laser absorption spectroscopy (TDLAS), Fourier transform infrared spectroscopy (FTIR), and small angle X-ray scattering (SAXS) experiments. The inset illustrates the basic shape of the nozzle, the static pressure probe and the location of the static pressure tap used to determine the stagnation pressure. The inset figure is not to scale and greatly exaggerates the opening angle of the nozzle.

controllers assure that the gas flow rate varies by less than ~3%. The combined gas mixture then flows through a heat exchanger placed in a temperature controlled water bath before entering the plenum. In the plenum, the velocity is low enough for the gas to be considered at rest. The temperature is further controlled by circulating water from the water bath through additional coils in the plenum, while the pressure in the plenum is controlled by adjusting the flow rate of gases through the nozzle. The stagnation temperature T_0 of the gas mixture is measured using a platinum resistance temperature detector (RTD) located in the center of the flow straightener near the plenum exit. The variation in the temperature measured by the RTD is held to less than ±0.05 K. The stagnation pressure p_0 is determined by measuring the static pressure *via* a pressure tap in the region of constant area of the nozzle and correcting for the gas velocity. Finally the gas mixture flows through the Laval nozzle before exiting the flow system through two rotary vane vacuum pumps with a combined pumping capacity of 0.13 m^3 s^{-1}.

The supersonic Laval nozzles are made of aluminium and have a rectangular cross section with flat sidewalls. As illustrated schematically in the inset of Fig. 1, the top and the bottom blocks define the expansion. The first 21 mm is a region of constant cross-section, followed by a 43 mm long converging and a 95 mm long diverging section. The channel width is ~12 mm, and at the throat the channel height is ~5 mm. The Mach number at the nozzle exit is ~1.8. Two different nozzles with the same nominal dimensions are used in this work. In the first nozzle, nozzle H, each side wall has a CaF_2 window (12 mm long × 6 mm high × 2 mm thick) in the region of constant cross-section and a second CaF_2 window with anti-reflective coating (90 mm long × 6 mm high × 2 mm thick) spanning the subsonic and supersonic regions of the nozzle (see Fig. 1). Nozzle H was used for the PTM, TDLAS, and FTIR experiments. The SAXS experiments were conducted using a second nozzle, nozzle H2, where each sidewall contains a 90 mm long × 1 mm high × 25 μm thick mica window that spans the same region of the flow as the large CaF_2 window in nozzle H. Both nozzles have the same linear expansion rate, $d(A/A^*)/dz = 0.059$ cm^{-1}. Although A^* differs slightly between nozzle H and H2, we compensate for this difference by adjusting the mass flow rates to maintain the same initial partial pressure of the condensible, p_{v0}, for the complementary experiments.

To make position resolved TDLAS, FTIR, and SAXS measurements, the plenum, supersonic nozzle, and part of the tubing are mounted on a translational stage that moves in the axial direction with 0.2 mm, or better, resolution.

C Pressure trace measurements (PTMs)

In a PTM experiment, we characterize the temperature T_0, pressure p_0, and composition of the gas mixture at the nozzle inlet and measure the axial static pressure distribution for both the non-condensing (carrier gas) and condensing (carrier gas + condensible vapor) flows using a sliding static pressure probe. In nozzle H2, we also measure the static pressure at the physical throat *via* a 0.34 mm diameter hole in the nozzle block. By comparing the pressure at the physical throat to the pressure measured by the static pressure probe, we obtain the distance between the physical throat and the effective throat. The effective throat is defined as the position where the effective area ratio reaches its minimum and the pressure ratio p^*/p_0 corresponds to a Mach number M equal to 1. For a gas mixture in which the heat capacity is a function of temperature, the value of p^*/p_0 is calculated using the integration scheme described in the appendix of Tanimura *et al.*[38] Since nozzle H does not have a pressure tap at the physical throat, the difference between the location of the physical throat and the effective throat in nozzle H is assumed to be the same as in nozzle H2. The distance between the physical throat and the effective throat is required to combine PTM data with TDLAS, FTIR, and SAXS data because the pressure profile is measured relative to the effective throat while the spectra from TDLAS, FTIR, and SAXS experiments are measured relative to the physical throat. From this point forward, the throat will always refer to the effective throat.

D Tunable diode laser absorption spectroscopy (TDLAS)

In TDLAS experiments, we determine the temperature of the gas mixture under both condensing and non-condensing conditions by measuring the rotational temperature of the methane seed gas. The details of the setup and the principles of operation have been described by Tanimura *et al.*[35,37,38] To summarize, our TDLAS setup uses a lead salt laser diode (Laser Component) housed in a liquid nitrogen Dewar to generate a single mode IR laser beam with a line width of 20 MHz. The laser frequency is tuned by changing the temperature and the current supplied to the laser diode. Once we identify a spectral region of interest, we scan the current at a constant temperature to obtain the spectrum, over a spectral range of ~1 cm^{-1}. An optical train focuses, collimates, and splits the laser beam. Part of the beam, the reference beam, passes through a 5 cm long reference cell containing methane before it reaches a mercury–cadmium–telluride (MCT) detector. This signal is used to lock the laser frequency. The main laser beam passes through the nozzle before it is reflected and focused by a pair of mirrors onto a second MCT detector. We translate the nozzle, with respect to the fixed laser beam, to measure absorption spectra at various axial positions in the nozzle.

During a TDLAS experiment, two CH_4 absorption lines at frequencies ν_1 and ν_2 and corresponding ground state energies E_1'' and E_2'' are measured for each axial position in the nozzle. We first measure the CH_4 line at ν_1 as a function of position in the nozzle and then repeat the process for the CH_4 line at ν_2 because it takes about 30 minutes for the frequency of the laser diode to stabilize after changing the laser diode temperature. For each CH_4 spectrum, a sample (N_2 + MeOH + CH_4) and a background (N_2 + MeOH) spectrum are measured for about 10 s each with a maximum of 45 s between the two measurements to minimize instrumental drift. The sample spectrum is then divided by the background spectrum to correct for laser intensity variation and fringes that originate from light reflected by the nozzle windows. Since the CH_4 mole fraction is the same for both position resolved measurements, we can use the relationship between the ratio of the

Table 1 The CH_4 absorption lines used in this work are characterized by the frequency ν in cm^{-1}, the intensity S at 296 K in $cm^{-1}/(molecule\ cm^{-2})$, the weighted transition moment squared R in debye, the air-broadening half width at 296 K γ_{air} in cm^{-1}/atm, the self-broadening half width at 296 K γ_{self} in cm^{-1}/atm, the lower state energy E'' in cm^{-1}, the coefficient of the temperature dependence of the air-broadened half width n_{air}, and the air-broadened pressure shift of the line transition at 296 K δ in cm^{-1}/atm. The data are from Rothman *et al.*[41]

Mol.	ν	S	R	γ_{air}	γ_{self}	E''	n_{air}	δ
CH_4	1360.15722	1.161×10^{-20}	3.190×10^{-3}	0.0577	0.0703	575.2598	0.73	−0.002093
CH_4	1332.08529	5.703×10^{-20}	3.794×10^{-3}	0.0625	0.0778	104.7800	0.69	−0.002049

absorbance areas of the two absorption lines, their energy, and temperature given by

$$\frac{I(\nu_1)}{I(\nu_2)} = \frac{S(\nu_{1,296})}{S(\nu_{2,296})} \exp\left[\frac{hc}{k_B}(E_1'' - E_2'')\left(\frac{1}{296} - \frac{1}{T_{TDLAS}}\right)\right], \quad (1)$$

to iteratively determine the temperature. In eqn (1) $I(\nu_\alpha)$ is the absorbance area, S is the line intensity at 296 K, and E_α'' is the energy of the lower state for the transition at ν_α, h is Planck's constant, k_B is Boltzmann's constant, and c is the speed of light. To start the iteration, the CH_4 absorbance areas are estimated by fitting the subtracted spectra to Voigt line shapes using the TDL Wintel software,[40] with the measured static pressure and the temperature estimated by PTM as input parameters. These two absorbance areas are then used in eqn (1) to update the temperature. The process is repeated using the new value of temperature and the measured static pressure until the temperature converges, usually within two iterations. The properties of CH_4 lines used in this study are summarized in Table 1. The two CH_4 lines are for the same isotopologue ($^{12}CH_4$).

In contrast to the temperature determined from the static pressure measurements, the temperature measured in TDLAS experiments, T_{TDLAS}, is the average temperature across the flow and includes contributions from the warmer gas in the boundary layers. Thus, when there is condensation in the nozzle, we can use the measured static pressure and T_{TDLAS} as inputs to iteratively solve the flow equations, using the scheme described in Tanimura *et al.*[36] to account for boundary layer compression. This improves our estimate of the centerline temperature over that determined from pressure measurements alone. From here on, the temperature T is the centerline temperature and the other flow properties are calculated based on this value.

E Small angle X-ray scattering (SAXS)

In SAXS experiments, we measure the small angle X-ray scattering from the MeOH aerosol as a function of position in the nozzle by moving the nozzle relative to the X-ray beam. At each position we measured the sample (N_2 + CH_4 + MeOH or N_2 + MeOH) and the background (N_2 + CH_4 or N_2). Two sets of SAXS experiments, in 2005 and 2007, were performed using the 12-ID_C beam line at the Advance Photon Source (APS),[42] Argonne National Labs. In both sets of measurements we used a 0.2 mm × 0.2 mm beam of 12 keV X-rays with a wavelength spread $\Delta\lambda/\lambda = 10^{-4}$. The range of scattering wave vector q_{SAXS}, defined by $q_{SAXS} = (4\pi/\lambda)\sin(\theta/2)$ where λ is the X-ray wavelength and θ is the scattering angle, was calibrated by scattering from a sample of silver behenate.[43–45] The APS data inversion program was used to reduce the two dimensional data and produce the radially averaged one dimensional spectra. This program accounts for the dark background, pixel efficiency, and spatial inhomogeneities on the detector.

In 2005, the nominal sample to detector distance (SDD) was 2 m and CH_4 was included in the gas mixture. At each position we used sample and background integration times of 5 s. The absolute calibration factor was determined by cross calibrating D_2O aerosol SAXS measurements to our earlier small angle neutron scattering (SANS) measurements conducted under identical conditions that were on an absolute intensity scale.[39] In 2007, the nominal SDD was 0.7 m, and CH_4 was not included in the flow. Separate PTM experiments confirmed that excluding CH_4 has a negligible effect. Sample and background integration times varied from 10 s to 100 s to improve measurements of the smallest droplets. The absolute calibration factor for the 2007 data was obtained[39] by forcing the condensed volume fraction from position resolved SAXS measurements of D_2O aerosol to agree with those derived from the TDLAS measurements of Paci *et al.*[37] and Tanimura *et al.*[35]

To characterize the MeOH aerosols generated in the supersonic flow, we fit the SAXS spectra to scattering from a Schultz distribution[46] of polydisperse spheres and obtained the average particle size $\langle r\rangle$, the size distribution width σ, and the scattering intensity as $q_{SAXS} \to 0$, I_0. For data on an absolute intensity scale, the aerosol number density N can be obtained from $\langle r\rangle$, σ, and I_0 using

$$N = \left(\frac{3}{4\pi}\right)^2 \left(\frac{(Z+1)^5}{(Z+2)(Z+3)(Z+4)(Z+5)(Z+6)}\right) \times \left(\frac{I_0}{\langle r\rangle^6 (\Delta\rho)^2}\right), \quad (2)$$

where $Z = (\langle r\rangle/\sigma)^2 - 1$ and $\Delta\rho$ is the difference in the scattering length densities of the condensed phase and the carrier gas. The aerosol volume fraction ϕ_l is given by

$$\phi_l = \frac{4\pi}{3}\frac{(Z+3)(Z+2)}{(Z+1)^2}\langle r\rangle^3 N, \quad (3)$$

while the aerosol mass fraction g_l is given by

$$g_l = \frac{\rho_l}{\rho}\phi_l, \quad (4)$$

where ρ is the density of the flowing gas mixture (carrier gas + monomer + clusters + droplets) and ρ_l is the methanol liquid density. We assume that the physical properties of the methanol droplets are the same as those of bulk liquid, but we ignore the change in density of the liquid due to the increased internal pressure of the droplet.

F Fourier transform infrared spectroscopy (FTIR)

In FTIR experiments, we measure the absorption spectra of MeOH as a function of axial position in the nozzle using a Perkin Elmer Spectrum 100 FT-IR spectrometer in absorption mode with an MCT detector. Since our flow system/nozzle setup does not fit in the measurement cavity of the FTIR spectrometer, we guide the IR beam through the nozzle using a series of mirrors consisting of 6 plane mirrors and 2 focusing mirrors with 20 cm focal length as shown in Fig. 2, and focus the beam so that it is 0.5 cm wide at our observation window. Since IR transmission through the CaF_2 window drops significantly at wavenumbers less than $\sim$1100 cm^{-1}, we measured the spectra with 1 cm^{-1} resolution and analyzed in the wavenumber range from 900 to 4000 cm^{-1}. At each position in the nozzle, we measure two 32 scan sample (N_2 + MeOH) spectra and two 32 scan background (N_2) spectra. The background-subtracted spectra are obtained using the Perkin-Elmer Spectrum version 6.3.4 software. Since the IR beam path is not purged during these measurements, the built-in CO_2/H_2O suppression subroutine is used to minimize CO_2 and H_2O absorption interference from the atmosphere in the background subtraction procedure.

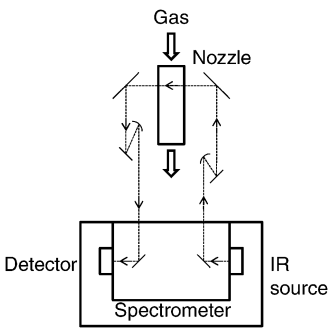

Fig. 2 A schematic (top view) of the FTIR setup integrated with the nozzle. The IR beam is focused at the center of the nozzle.

G Chemicals and thermophysical properties

The methanol used in the experiments (Sigma-Aldrich CHROMASOLV Plus) had a purity $\geq$ 99.9%. The methane gas purity was 99.97%. The carrier gas was nitrogen with purity $\geq$ 99.99%. The thermophysical properties of the chemicals used are summarized in Table 2.

III. Results and discussion

We performed PTM and TDLAS experiments to characterize the non-condensing (N_2 + CH_4 or N_2) flow while all four experimental techniques were used to characterize the condensing (N_2 + CH_4 + MeOH or N_2 + MeOH) flows. The condensing flow experiments were conducted at methanol initial partial pressures, p_{v0}, of 0.87, 1.26, and 2.09 kPa. For all experiments, the stagnation pressure p_0 was 59.6 kPa, the stagnation temperature as measured by the RTD in the plenum $T_{0,RTD}$ was 35.0 °C, and the effective throat was consistently 0.11–0.12 cm downstream of the physical throat. For the TDLAS experiments we determined T_0 by forcing $\langle T \rangle_{laminar}$, the average temperature across the flow estimated from the PTM and laminar boundary layer theory, to match T_{TDLAS} near the throat—a region where neither condensation nor clustering occurs. Table 3 summarizes the experimental conditions including the values of T_0 determined for the TDLAS experiments.

Table 3 A summary of the experimental conditions including the methanol initial partial pressures p_{v0}, stagnation temperatures in TDLAS experiments $T_{0,TDLAS}$, and the distance of the effective throat from the physical throat Δz. The stagnation pressure p_0 for all experiments was maintained at 59.6 kPa, while the stagnation temperature T_0 for all experiments other than TDLAS were assumed to be at 35.0 °C based on $T_{0,\ RTD}$

p_{v0}/kPa	$T_{0,TDLAS}$/°C	Δz/cm
0	33.2	0.11
0.87	31.6	0.11
1.26	32.0	0.11
2.09	32.2	0.12

Table 2 The thermophysical properties of methanol, methane, and nitrogen. The properties are the molecular weight μ, the vapor molar heat capacity at constant pressure C_{pv}, the liquid density ρ_l, the enthalpy of vaporization ΔH_{vap}, the dimer and tetramer dissociation enthalpies, ΔH_2 and ΔH_4, respectively, the dimer and tetramer dissociation entropies, ΔS_2 and ΔS_4, respectively, and the universal gas constant R = 8.314 J mol^{-1} K^{-1}

		Refs./notes
Methanol		
μ/g mol^{-1}	32.04	
C_{pv}/J mol^{-1} K^{-1}	$42.311 - 5.1838 \times 10^{-2}T + 1.9314 \times 10^{-4}T^2$	*a*
ρ_l/kg m^{-3}	$1153.6 - 1.9319\ T + 3.7371 \times 10^{-3}T^2 - 4.6487 \times 10^{-6}T^3$	*b*
ΔH_{vap}/J mol^{-1}	$R\ (6341.27 - 5.67\ T)$	*c*
ΔH_2/cal mol^{-1}	3220	3
ΔS_2/cal mol^{-1} K^{-1}	16.5	3
ΔH_4/cal mol^{-1}	24200, 23600	3,6
ΔS_4/cal mol^{-1} K^{-1}	81.3, 80.49	3,6
Methane		
μ/g mol^{-1}	16.04	
C_{pv}/J mol^{-1} K^{-1}	$R\ (4.3370 - 3.7677 \times 10^{-3}T + 9.1107 \times 10^{-6}T^2 + 1.0178 \times 10^{-9}T^3)$	*d*
Nitrogen		
μ/g mol^{-1}	28.01	
C_{pv}/J mol^{-1} K^{-1}	29.124 (at 298.15 K)	47

[a] Methanol C_{pv} is a quadratic fit to data in Goodwin[48] for $150 < T/K < 300$. [b] Methanol ρ_l is a cubic fit to data in Goodwin[48] for $180 < T/K < 320$. [c] Methanol ΔH_{vap} is determined from applying the Clausius–Clayperon equation to the vapor pressure data in Schmeling and Strey[49] for $243.2 < T/K < 303.2$. [d] Methane C_{pv} is a cubic fit to data in McDowell and Kruse[50] for $160 < T/K < 340$.

In all cases we found that T_0 was less than $T_{0,RTD}$ and we attribute the difference to bypass flow inside the plenum as described by Tanimura *et al.*[38] Since the SAXS and FTIR experiments were conducted after the bypass flow issue was resolved, we assume that T_0 = 35.0 °C for those measurements. Although one can adjust the data for small changes in T_0 between different experiments, as described in Appendix D of Tanimura *et al.*,[36] the net effect of this procedure is minimal: the data taken at higher temperature are shifted downstream by ~0.2–0.3 cm relative to the data measured at lower T_0. The other major effect of the uncertainty in temperature is to introduce 1–2% uncertainty into the density of the gas phase, a correction that is negligible for the analysis in this paper. Thus, we present the data as they were measured and acknowledge that there is a somewhat larger discrepancy in T_0 between experiments than we would prefer.

A Pressure and temperature measurements

Fig. 3 illustrates the pressure ratios (lower curves) and temperature profiles (upper curves) measured for the non-condensing and condensing flows as a function of position, z, where z = 0 corresponds to the throat. For the non-condensing flow, Fig. 3(a), the solid gray line is the measured pressure ratio p/p_0 while the solid black line is the gas temperature at the flow centerline, where, in this case, the centerline temperature is derived from p/p_0 assuming an isentropic expansion. The black dotted line represents $\langle T\rangle_{laminar}$, the average temperature calculated from the PTM assuming a laminar boundary layer develops along the nozzle walls. Finally, the open circles correspond to the measured temperatures, T_{TDLAS}. For the non-condensing flow, the values of T_{TDLAS} generally agree with $\langle T\rangle_{laminar}$ to better than 2 K. The accuracy of the current T_{TDLAS} measurements is somewhat lower than those of Tanimura *et al.*[38] This is most likely because our experiments are at higher pressure where the CH_4 lines are broader and not as easy to fit. Nevertheless, Fig. 3(a) confirms the conclusion of Tanimura *et al.*[35] that laminar boundary layer theory adequately explains the observed differences between the centerline temperature T and the average temperature of the flow measured by spectroscopy, T_{TDLAS}.

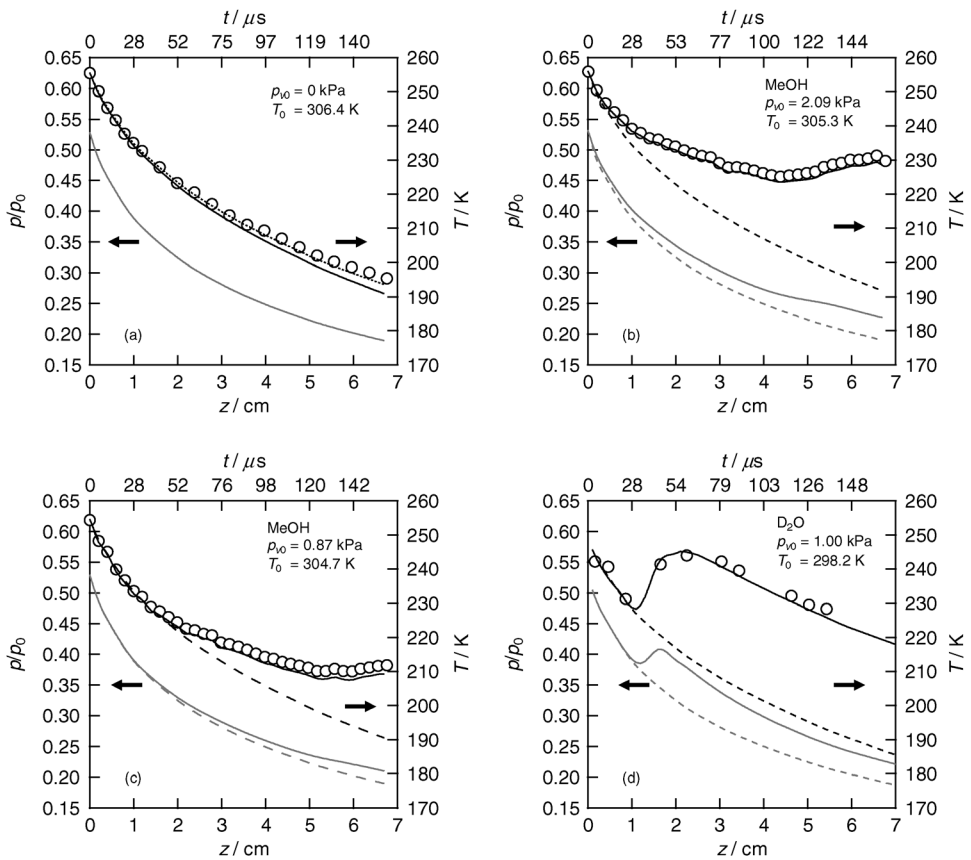

Fig. 3 The measured pressure ratios and temperatures for the (a) non-condensing flow, (b), (c) condensing flows of dilute MeOH mixtures, and (d) condensing flow for a comparable D_2O mixture.[35] The upper axes give the flow time corresponding to the values of z on the lower axis, where $z = t = 0$ corresponds to the throat. In (a)–(c) expansions started from p_0 = 59.6 kPa and the other experimental conditions are noted in each figure. In (d) the expansion started from p_0 = 60.4 kPa. The solid gray lines are the measured pressure ratios p/p_0, while the dashed gray lines are those expected for an isentropic expansion of the gas mixture in the absence of vapor phase association. The open circles, black dashed lines, and black solid lines, represent T_{TDLAS}, the expected temperature for an isentropic expansion of the gas (no clustering), and the centerline temperature T, respectively. For the condensing flows, (b)–(d), T was calculated as described in Section IID or in ref. 35. For the non-condensing flow, (a), T was calculated assuming an isentropic expansion. The black dotted line in (a) represents $\langle T\rangle_{laminar}$, the average temperature calculated from the PTM assuming a laminar boundary layer develops along the nozzle walls. The corresponding figure for the third MeOH condensation experiment, where p_{v0} = 1.26 kPa, is available in ESI.†

The lines and symbols for the condensing flow experiments are the same as for the non-condensing flow. The centerline temperatures (black solid lines) for MeOH were derived by solving the adiabatic flow equations (see Appendix) with pressures from PTM experiments and temperatures from TDLAS experiments as inputs.[51] In addition, the dashed gray (black) lines illustrate the pressure ratios (temperatures) expected for an isentropic expansion of this gas mixture in the absence of vapor phase association. In a more typical vapor, for example, D_2O, as illustrated in Fig. 3(d), the pressure ratio and temperature profiles of the condensing flow closely follow those of the isentropic expansion before deviating significantly, as heat is released to the surrounding gas due to droplet growth. Furthermore, monomer depletion, droplet formation and droplet growth all occur relatively quickly ($\sim$25 μs) compared to the flow time in the supersonic portion of the nozzle ($\sim$160 μs). As illustrated for the condensing MeOH flows in Fig. 3, the pressure ratio and temperature profiles measured for the expansion of this vapor mixture behave quite differently. Although for each p_{v0} there is a short region where the measured pressure ratios and temperature closely follow the expected isentropic expansion, for MeOH the initial deviation of the measured condensing flow profiles from the corresponding isentropic values is both rather gentle and prolonged. Further downstream, there is larger and more significant deviation that begins after the minimum temperature. A simple explanation of this behavior is that the initial gentle deviation stems from heat release due to the formation of small MeOH clusters, while the more significant heat release further downstream is due to rapid droplet growth. The difference in behavior between methanol and water (D_2O) is consistent with the fact that methanol associates more strongly in the vapor phase than water or the longer chain length *n*-alcohols.[52]

To determine whether this interpretation is valid requires additional information. We begin by experimentally determining the mass fractions of the methanol monomer and droplets as functions of position.

B Methanol monomer mass fraction

The OH stretching frequency is a sensitive probe to distinguish between monomer, clusters, and liquid methanol. In the monomer, the OH bond stretches freely and the absorption feature is in the wavenumber range $3600 < \nu/\mathrm{cm}^{-1} < 3800$. When hydrogen bonds form between methanol molecules, the frequency of the OH stretching vibration is reduced, the absorption peak shifts to lower wavenumber, $3100 < \nu/\mathrm{cm}^{-1} < 3600$, and this peak is clearly separated from absorption due to the monomer. FTIR spectra confirm that there is no signal in the hydrogen bonded region at the nozzle throat. Thus, at $z = 0$ cm all methanol molecules are monomers and we can use the free OH absorption spectrum measured there as a reference spectrum with which to fit this region of the spectrum at any other position in the nozzle. Prior to condensation the mass fraction of monomer is known because the flow rates of carrier gas and condensible entering the nozzle are measured. As illustrated in Fig. 4(a), for example, after dividing by a scaling factor of 1.6 the free OH absorption spectrum at $z = 0$ cm is in good agreement with the spectrum at $z = 2$ cm. Since the spectrum at $z = 0$ cm is measured at $\sim$23 K higher than the spectrum at $z = 2$ cm, the good agreement means the temperature dependence of this region of the monomer spectrum is negligible under our experimental conditions. Thus, the mass fraction of methanol monomer at a given position in the nozzle $g_{\mathrm{mono}}(z)$ can be estimated from the mass fraction of methanol monomer at the throat $g_{\mathrm{mono}}(0)$ and the scaling factor $SF(z)$ by

$$g_{\mathrm{mono}}(z) = \frac{g_{\mathrm{mono}}(0)}{SF(z)} \times \frac{\rho(0)}{\rho(z)}, \qquad (5)$$

where the density ratio ($\rho(0)/\rho(z)$) corrects for the continued expansion of the gas mixture and is determined from the pressure and temperature measurements.

Fig. 4(b) summarizes the methanol monomer mass fractions determined from the FTIR measurements. In each case there is a short region near the throat where the monomer concentration is constant that corresponds to the region where the condensing flow follows the isentropic expansion. The monomer concentration then decreases continuously with increasing z as the monomer is consumed to form small *n*-mers and/or droplets.

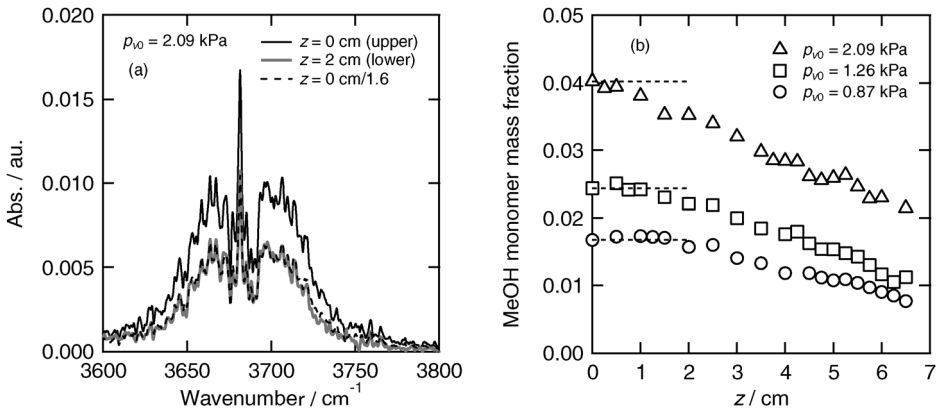

Fig. 4 (a) The free OH region of the methanol spectrum measured at $z = 2$ cm is fit by scaling the spectrum at $z = 0$ cm by a factor of 1.6. The experimental conditions are noted in the legend. (b) The MeOH monomer mass fraction determined from FTIR experiments for p_{v0} at 2.09, 1.26, and 0.87 kPa. The dashed line corresponds to the measured MeOH mass fraction entering the nozzle.

C Methanol liquid mass fraction

One way to ascertain the appearance of the droplets, follow their subsequent growth, and determine the liquid mass fraction during methanol condensation is to conduct *in situ* SAXS experiments. Fig. 5 shows several position resolved aerosol SAXS spectra for the highest initial partial pressure, p_{v0} = 2.09 kPa, from measurements taken in 2005. The spectrum at z = 6.5 cm is on the absolute intensity scale while the spectra at z = 5.5 and 4.5 cm are offset for clarity by factors of 10^{-1} and 10^{-2} respectively. As z decreases, the inflection point in the intermediate q_{SAXS} range moves towards larger q_{SAXS} while the spectra become noisier. Both observations are consistent with decreasing droplet size. Upstream of z = 4.2 cm, the SAXS spectra are too noisy to fit. Either there are no droplets or the droplets are too small and the aerosol number density is too low for X-rays to scatter with enough intensity to be observed above the background. For the spectra we could fit, we determine the droplet mean radius $\langle r \rangle$, the width of the size distribution function σ, and droplet number density N by fitting scattering from a Schultz distribution of polydisperse spheres to each spectrum. The fit parameters noted in Fig. 5 correspond to the black solid line running through the top spectrum in the figure and illustrates a typical Schultz fit to the SAXS spectrum at z = 6.5 cm.

Fig. 6(a)–(c) summarize the fit results of the 2005 and 2007 measurements for the three MeOH partial pressures, and the corresponding table of values is available as ESI.† The SAXS measurements made two years apart using different detectors, different sample to detector distances, and distinct absolute calibration procedures are in excellent agreement. The locations where droplet size distributions can first be fit are ~4.2, 4.7, and 5.4 cm downstream of the throat for p_{v0} = 2.09, 1.26, and 0.87 kPa, respectively. The mean droplet size increases rapidly, while the width of the distribution σ increases more slowly, by only 30–35% overall. At the same time, N initially increases before leveling off with increasing z. The droplet mass fraction, calculated using eqn (3) and (4), and illustrated in Fig. 6(d), also increases rapidly with increasing z. For the current setup, the smallest droplets whose scattering spectra we can reasonably fit have average radii $\langle r \rangle \approx$ 3.7 nm and contain ~3400 monomers, while the minimum droplet mass fraction we can detect is $\sim 7.3 \times 10^{-4}$. Furthermore, we note that the locations where we can first reliably observe SAXS spectra and the regions of rapid droplet growth are consistent with the locations of the temperature minima and the increases in temperature observed in the temperature profiles, respectively, as seen in Fig. 3. The increase in N during the early stages of droplet growth is also consistent with continued nucleation before the rapid increase in temperature quenches nucleation completely.[53]

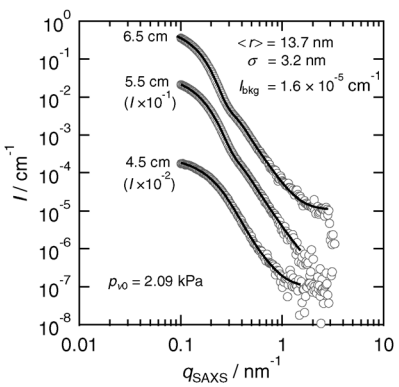

Fig. 5 The SAXS spectra of the methanol droplets were measured at several positions in the nozzle for p_{v0} of 2.09 kPa MeOH. The spectrum at z = 6.5 cm is at the true absolute intensity while the spectra at z = 5.5 and 4.5 cm are offset by 10^{-1} and 10^{-2}, respectively, for clarity. The fit parameters correspond to the solid line drawn through the spectrum measured at z = 6.5 cm. The parameters corresponding to the fits at 4.5 and 5.5 cm are available in the ESI.† I_{bkg} is a flat background that arises from scattering of the gas along the X-ray path and its density fluctuations.

D The methanol species distribution

With the methanol monomer and liquid mass fraction determined, we can estimate the mass fraction of small n-mers by mass balance, *i.e.*, by subtracting the sum of the monomer and liquid mass fractions from the mass fraction of methanol entering the nozzle. Fig. 7 illustrates the methanol distribution between monomer, clusters, and liquid droplets during the expansions with p_{v0} = 2.09, 1.26 and 0.87 kPa. In all three cases, there is a short region where the monomer mass fraction is constant before it decreases steadily throughout the remaining expansion. As noted earlier, the liquid first appears near z = 4.2, 4.7, and 5.4 cm for p_{v0} = 2.09, 1.26, and 0.87 kPa, respectively, and then increases rapidly. Finally, the cluster mass fraction is initially zero, increasing as the monomer concentration decreases. The cluster concentration is maximized close to the position where the liquid first appears, and then it decreases and disappears as the liquid mass fraction increases rapidly. The slightly negative values for the cluster mass fractions near the nozzle exit arise from a slight overestimation of either the vapor or liquid mass fraction. At the nozzle exit the SAXS scattering signal is very strong and there is very good agreement between independent measurements. In contrast, the FTIR signal is getting progressively weaker due to depletion and continued expansion. We, therefore, suspect that in this region of the nozzle the monomer mass fraction measured by the FTIR is more likely to be in error than the SAXS measurement.

The mass fraction profiles of monomer, clusters, and liquid during expansion support the simple explanation proposed in Section IIIA, *i.e.*, clusters form first, consuming monomer and releasing heat that causes the temperature and pressure ratio to gently deviate from the expected isentropic expansion. The clusters continue to form until liquid droplets, containing more than ~3400 monomers, begin to appear at a position that is consistent with the location where we observe a stronger increase in temperature and an inflection in the pressure ratio. Once liquid droplets form, they grow rapidly consuming the monomer and the clusters. The increase in number density observed in our SAXS measurements also suggests that there is a region where droplet formation and growth occur simultaneously. Despite the detailed level of information obtained by these measurements, the average size of the clusters is still unknown.

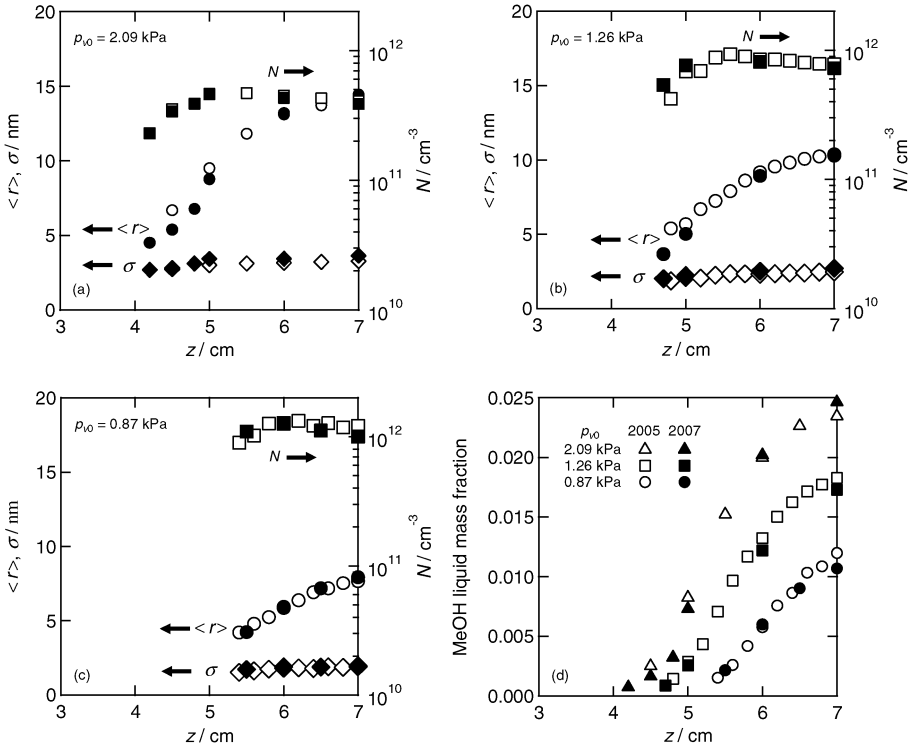

Fig. 6 The mean radius, $\langle r \rangle$, the width of the distribution function, σ, and the droplet number density, N, as a function of position in the nozzle for (a) p_{v0} = 2.09 kPa MeOH, (b) p_{v0} = 1.26 kPa MeOH, and (c) p_{v0} = 0.87 kPa MeOH. The open symbols correspond to measurements made in 2005 while the filled symbols correspond to measurements made in 2007. (d) The liquid mass fraction, g_l, as a function of position for all values of p_{v0} measured in position resolved SAXS experiments.

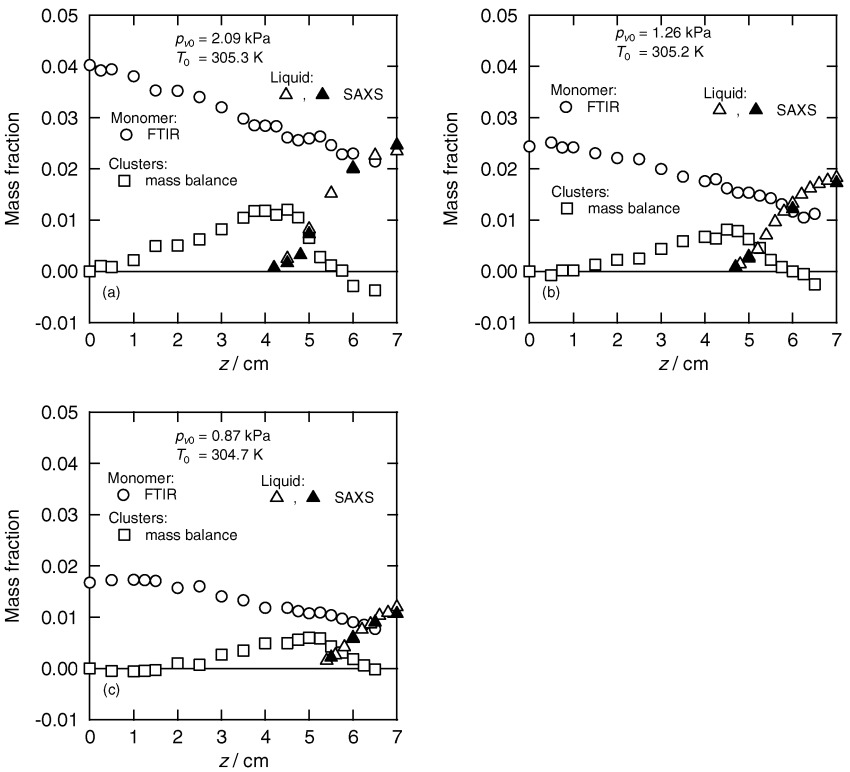

Fig. 7 Methanol species distribution estimated from FTIR and SAXS experiments for (a) p_{v0} = 2.09 kPa MeOH, (b) p_{v0} = 1.26 kPa MeOH, and (c) p_{v0} = 0.87 kPa MeOH. The cluster mass fraction is estimated by mass balance. In all three cases, the monomer mass fraction is initially constant before decreasing continuously as monomer is consumed, first to form clusters and then to form droplets. The cluster mass fraction increases, reaching a maximum near the point where the liquid first appears, and then decreases as the liquid droplet mass fraction grows.

E Models of the methanol species distribution and the average heat release

One possibility for estimating the cluster size is to use the supersonic flow model to tie together the pressure, temperature, and the methanol species distribution measurements in a self-consistent manner. To summarize, the model combines equations describing condensation in supersonic flow with a thermochemical equilibrium model to account for vapor association. The measured static pressure and temperature are the input variables. The model then estimates the distribution of methanol species in the gas mixture and the average heat release due to cluster and droplet formation and growth. Three different versions of the model were investigated. Model I assumes that the gas mixture consists of carrier gas, monomer, and liquid only. This is our standard model that has been presented many times[34,35] and that accurately describes the condensation of molecules like D_2O.[35,37] Although we do not expect this model to adequately describe the flow, it is instructive to include it as a base case. Model II assumes that the gas mixture consists of carrier gas, monomer, dimer, tetramer, and liquid. We explore two versions of this model to test the sensitivity of the model to the equilibrium constants for cluster formation. The constants are obtained either from fitting heat capacity data,[3] Model II(i), or thermal conductivity data,[6] Model II(ii). Model II(ii) was used by Strey *et al.*,[32,54] and Peters and Paikert[33] to account for vapor association in their methanol nucleation rate experiments. Preliminary investigation of a third model, one that assumes the gas mixture consists of carrier gas, monomer, trimer, octamer, and liquid, with cluster formation equilibrium constants obtained from vapor pressure measurements,[11] showed that monomer depletion was severely overestimated. For the case of p_{v0} = 2.09 kPa at z = 1 cm, for example, this equilibrium model predicts a monomer concentration that is ~30% lower than the FTIR measurement due to rapid formation of the octamer. Consequently, this model was not pursued further.

Fig. 8(a)–(c) illustrate the results and compare the predicted distributions of monomer, clusters and liquid to those derived from FTIR and SAXS measurements. All models predict that the methanol monomer mass fraction decreases continuously with z and all predictions are generally within 6% of the FTIR measurements except near the nozzle exit. In fact, the predicted monomer mass fractions differ by less than 6% from each other, although the absolute deviations between the model and

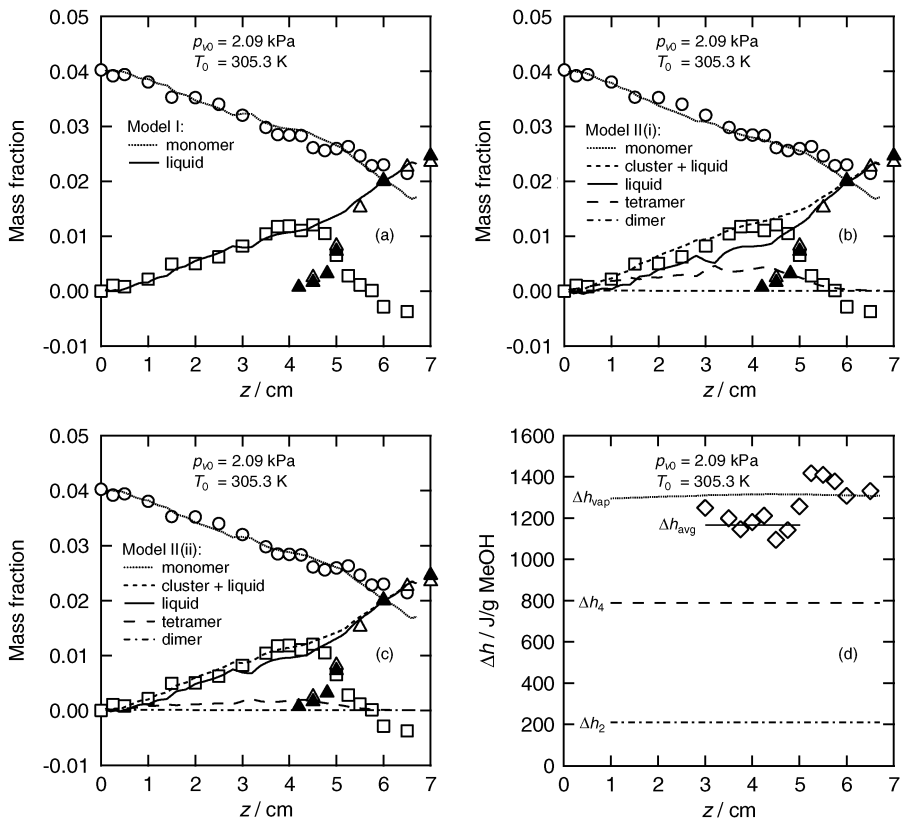

Fig. 8 The methanol species distribution for p_{v0} = 2.09 kPa MeOH estimated using (a) model I, (b) model II(i), and (c) model II(ii) are compared to the monomer mass fraction determined by FTIR (○), the cluster mass fraction estimated by mass balance (□) and the liquid mass fraction determined by SAXS (△ and ▲ correspond to measurements made in 2005 and 2007, respectively). In all cases, the liquid mass fractions predicted by the models near the nozzle exit are in good agreement with the SAXS measurements. In contrast, the predicted cluster concentrations are almost everywhere too low. (d) depicts Δh_{avg}, estimated as the total heat released to the flow divided by the mass fraction of clusters + liquid. We consider only points where the total heat released and the mass fraction of clusters + liquid are high enough to prevent excessive noise for p_{v0} = 2.09 kPa. The solid line corresponds to the average value of the data points between $3 \leq z/\text{cm} \leq 4.75$ cm, 1175 J g^{-1}. The methanol liquid specific heat of vaporization Δh_{vap}, tetramer specific heat of dissociation Δh_4, and dimer specific heat of dissociation Δh_2 are ~1300, 789, and 210 J g^{-1} MeOH respectively.

the FTIR data are minimized for Model II(i). The large difference in monomer mass fractions between the model predictions and the FTIR data near the exit are consistent with our concerns that the FTIR measurements are not as accurate in this region of the nozzle. In contrast, the predicted methanol liquid mass fractions are in a good agreement with SAXS measurements near the nozzle exit.

None of the models, however, agree with the SAXS data on the location of the initial appearance of the liquid. This result is not unexpected for model I, because this model can only assign the observed heat released to liquid formation. Nevertheless, it is surprising that there is no SAXS signal observed when the mass fraction of monomer depleted from the vapor phase is as high as 1.1×10^{-2}, since liquid mass fractions as low as 7.3×10^{-4} can be detected. Signal to noise calculations, using the experimentally determined background, suggest that the depleted monomer would have to be distributed in an aerosol of droplets with an average radius less than $\sim$0.45 nm and a number density greater than $\sim 7.4 \times 10^{15}$ cm^{-3}. Such small "droplets" would contain at most 6 monomers, and in this paper we would consider them clusters.

In model II, we account for cluster formation *via* a monomer–dimer–tetramer equilibrium model in the vapor phase. If model II describes cluster formation in the nozzle correctly, we would expect the model to predict the measured monomer and liquid mass fractions correctly throughout the expansion with the remaining methanol distributed between dimer and tetramer. As illustrated in Fig. 8(b) and (c), both versions of model II predict that dimer concentrations are negligible throughout, but differ in the predicted concentrations of tetramer and liquid.

The equilibrium constants[3] used in Model II(i), predict higher tetramer concentrations than the equilibrium constants[6] used in Model II(ii). In Model II(i) tetramers appear shortly downstream of the throat, around $z = 0.1$ cm. Near $z = 4$ cm, tetramers reach a maximum mass fraction of 4.0×10^{-3} or $\sim$30% of the measured mass fraction of clusters, before decreasing to zero near the exit. Since this level of tetramer cannot account for the observed heat release, the model starts to produce "liquid" near $z = 1$ cm, well before droplets are observed in the SAXS measurements so that eqn (A8) is satisfied. One way to interpret the early appearance of the "liquid" is to assume that it corresponds to clusters larger than the tetramer but still smaller than the critical clusters that can grow spontaneously at the given methanol supersaturation, *i.e.* smaller than the critical nuclei that would initiate the vapor-to-liquid phase transition. For the conditions in this expansion, classical nucleation theory predicts the critical cluster size decreases from 82 at $z = 1$ cm to 24 at $z = 4.3$ cm. Since cluster size is expected to increase as the flow moves downstream, we can take the smallest critical cluster size as an upper bound for clusters throughout the nozzle.

We can directly estimate the specific average heat of dissociation of the clusters, or clusters + liquid, Δh_{avg}, by simply dividing the total heat released to the flow, q (in units of J g^{-1} gas mixture), by the mass fraction of methanol in the cluster and liquid state (in units g methanol per g gas mixture). The value of q is determined by solving the adiabatic flow equations with measured pressure and temperature as inputs and is insensitive to any underlying assumptions regarding the distribution of methanol. In this calculation, we assume that the cluster mass fraction is zero for the last two points near the exit and normalize the liquid mass fraction based on SAXS because we suspect the FTIR methanol monomer measurements near the exit are not as accurate. Fig. 8(d) summarizes the results of this calculation for the experiments with the highest methanol partial pressure, for conditions where both q and the mass fraction of clusters + liquid are high enough to be free of excessive noise. The value of Δh_{avg} stabilizes at $\sim$1175 J g^{-1} MeOH between $z = 3$–4.75 cm, where the cluster mass fraction is near its maximum value and where the liquid mass fraction is less than 3.2×10^{-3}. Further downstream, as the liquid mass fraction increases, the value of Δh_{avg} increases and converges to Δh_{vap} near the nozzle exit, where Δh_{vap} denotes the specific heat of vaporization of methanol liquid.

Theoretical calculations[22,23] clearly indicate an increase in the dissociation enthalpy with cluster size although they differ on the absolute values and the size of the cluster required before the dissociation enthalpy of the bulk liquid is reached. The fact that Δh_{avg} stabilizes between Δh_4 and Δh_{vap} suggests there are clusters larger than tetramer and smaller than the critical size, with a specific heat of dissociation that lies somewhere between the experimental values[3,6] reported for the tetramer, Δh_4, and that of the liquid, Δh_{vap}.

Finally, we note that it should be possible to use the data in Fig. 3 and 7 to extract and optimize equilibrium constants—including enthalpies and entropies of dissociation—for different underlying gas mixture models by applying an approach similar to that developed by Tucker *et al.*[11] to analyze methanol vapor pressure data. In particular, one could choose a model and optimize the constants to best fit the three distinct pressure–temperature data sets while adding necessary constraints to eliminate unphysical behavior such as negative equilibrium constants. This approach will not be attempted here as it is well beyond the scope of the current study.

F Distinguishing methanol clusters from liquid

To confirm the presence of the small clusters directly we can examine the IR absorption in the hydrogen bonded OH stretch region of the FTIR spectra more carefully. As is well documented,[15,27,55] when the OH group in a methanol cluster or in the liquid participates in a hydrogen bond, the OH stretching frequency is shifted to lower values and the magnitude of the shift increases with increasing strength of the hydrogen bonding environment. At the temperatures in our experiments, the cluster and liquid spectra are expected to overlap significantly. Nevertheless the liquid should still have absorption features at lower wavenumbers than the clusters.

To properly account for changes in absorption intensity due to changes in the number of absorbers (clusters and liquid droplets) in the path of the IR beam, we must first account for changes in the mass fraction of methanol in the clusters and liquid, g_{c+l}, and the density of the gas mixture. We chose our reference conditions to correspond to a position near the exit of the nozzle at $z_r = 6.5$ cm because we expect the cluster concentration to be negligible there and we have an independent estimate for the liquid mass fraction from the SAXS

experiments. Thus, we determined the scaled absorption $A_s(z)$ from the absorption measured at each position, $A(z)$, using,

$$A_s(z) = A(z) \times \frac{\rho(z_r)}{\rho(z)} \times \frac{g_{c+l}(z_r)}{g_{c+l}(z)}. \quad (6)$$

The values of $g_{c+l}(z)$ in eqn (6) are predicted using model II(i) because the model estimate of the monomer mass fraction gives the best agreement with FTIR measurements throughout most of the expansion, and the estimates for the total cluster and liquid mass fraction are in good agreement with SAXS measurements near the nozzle exit.

Fig. 9(a)–(c) illustrate how the scaled hydrogen bonded OH spectra change as the gas mixture flows through the nozzle for $p_{v0} = 2.09$ kPa. The spectra measured between the throat and $z = 1$ cm are not shown because the signal to noise ratio is too low. The remaining spectra fall quite naturally into three different groups. Fig. 9(a) illustrates the first group, corresponding to spectra measured between $z = 1$ cm and $z = 3$ cm downstream of the throat. Here the peak in the absorption intensity systematically shifts to lower wavenumber as z increases, and the scaled intensity increases by about 10%. Fig. 9(b) illustrates the second group that corresponds to measurements made when $3 < z/\text{cm} < 4$. The four scaled spectra shown here are essentially identical. Finally, Fig. 9(c) illustrates the third group of spectra measured when $4 < z/\text{cm} < 6.5$, the region that corresponds to the appearance of the liquid in the SAXS experiments. Here changes to the scaled spectra are quite dramatic. As z increases, the peak intensity decreases rapidly, the spectra broaden, and there is an isosbestic point at ~ 3250 cm^{-1}. Fig. 9(d) summarizes the wavenumber corresponding to the peak intensity of each spectrum as a function of position in the nozzle: up to $z = 3$ cm the location of the absorption peak is systematically red-shifted with increasing z, beyond this point it remains approximately constant. Although not shown here, very similar behavior was observed for the experiments conducted at the other methanol partial pressures.[57]

We interpret the behavior observed for the $p_{v0} = 2.09$ kPa experiment as follows. In the earliest stages of condensation, $1 < z/\text{cm} < 3$, both the cluster sizes and the cluster concentrations are changing rapidly. The systematic shift in the peak wavenumber is consistent with an increase in the average size of the clusters. Since absorption intensity is also a function of the hydrogen bond environment,[56] it is not surprising that the intensities of the scaled spectra are not constant. In the second stage of condensation, the consistency of the spectra illustrated in Fig. 9(b) demonstrates that in this region of the nozzle the absolute intensity scales well with the amount of

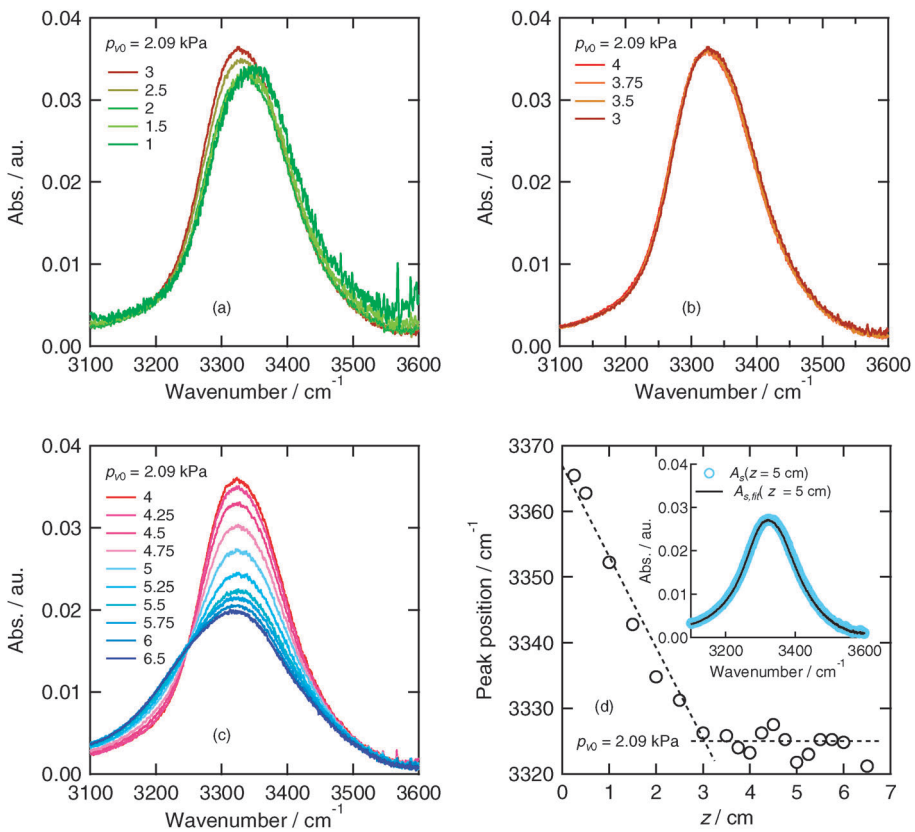

Fig. 9 (Color online) Methanol spectra in the hydrogen bonded OH stretch region for the experiment starting with $p_{v0} = 2.09$ kPa. The spectra have been adjusted for the concentration of hydrogen bonded methanol using eqn (6). (a) For $1 < z/\text{cm} < 3$ the cluster size and mass fraction of OH bonded MeOH both increase. (b) For $3 < z/\text{cm} < 4$ the scaled spectra overlap. (c) For $4 < z/\text{cm} < 6.5$ there is a steady transformation between the "cluster" state and the liquid state. The latter is characterized by a broader absorption peak with additional contributions at lower wavenumbers. (d) For $z < 3$ cm, the location of the peak shifts systematically to lower wavenumbers. For $z > 3$ cm, the location of the peak of the spectrum varies by less than ± 5 cm^{-1}. The inset in (d) shows the fit to the intermediate spectrum, at $z = 5$ cm, to a linear combination of the cluster reference spectrum at $z = 4$ cm and the liquid reference spectrum at $z = 6.5$ cm.

methanol in the clusters. One explanation of this behavior is that after the cluster distribution develops, the size distribution of clusters remains roughly constant while the mass fraction of clusters continues to increase. Alternatively, theoretical calculations[23] suggest that above a certain cluster size the heat of dissociation of the clusters is essentially constant and the position of the absorption peak in the hydrogen bonded OH stretch region of the infrared spectra no longer changes.[23] The limited experimental IR spectra measured for size resolved clusters[15] also suggest that it is difficult to determine cluster size from the OH stretch region of the IR spectrum alone once clusters contain more than 4 or 5 molecules. This is especially true if there is a distribution of cluster sizes present. Although our current experiments cannot distinguish small changes in the average size of the clusters during this stage of condensation, it seems reasonable to assume that the average cluster size is still increasing since the temperature is decreasing, and, eventually, critical clusters form to initiate the vapor–liquid phase transition. Finally, the appearance of the isosbestic point in Fig. 9(c) indicates that in this region of the nozzle there is a transition between two distinct states, or in our case, a transition between two hydrogen bonding environments. Since these spectra were measured in the region where the liquid first appears in the SAXS experiments we interpret the two states as corresponding to the cluster state and the liquid state.

We can take advantage of the isosbestic point to estimate the intermediate cluster and liquid mass fractions in the nozzle during the phase transition in the following manner. First, we assume that for the spectrum in Fig. 9(c) at $z = 6.5$ cm, A_{sl}, corresponds to pure liquid, and that for the IR spectrum measured just prior to the appearance of the liquid in SAXS (at $z = 4$ cm in Fig. 9(c)) A_{sc}, corresponds only to clusters. We then fit the scaled spectra at intermediate positions to a linear combination of these two spectra using

$$A_{s,fit}(z) = c_c(z) \times A_{sc} + c_l(z) \times A_{sl}, \quad (7)$$

where $c_c(z)$ and $c_l(z)$ are the fit constants, the fitting region is from 3100 to 3600 cm^{-1}, and the sum of $c_c(z)$ and $c_l(z)$ is constrained to equal 1. The inset in Fig. 9(d) illustrates the fit to the scaled spectrum at $z = 5$ cm.

The intermediate cluster and liquid mass fractions, $g_{c,FTIR}$ and $g_{l,FTIR}$ are then determined from

$$g_{c,FTIR}(z) = c_c(z) \times g_{c+l}(z)$$

and

$$g_{l,FTIR}(z) = c_l(z) \times g_{c+l}(z), \quad (8)$$

Fig. 10 summarizes the intermediate methanol cluster and liquid mass fractions derived by fitting the hydrogen bonded OH spectra and compares these to the values determined by the other measurement techniques at all three values of p_{v0}. For the clusters there is good agreement between $g_{c,FTIR}$ and the values based on mass balance, while for the liquid $g_{l,FTIR}$ and g_{SAXS} agree very well. The self consistency of these results is very encouraging and confirms that by using FTIR we are able to distinguish the presence of clusters from the presence of liquid.

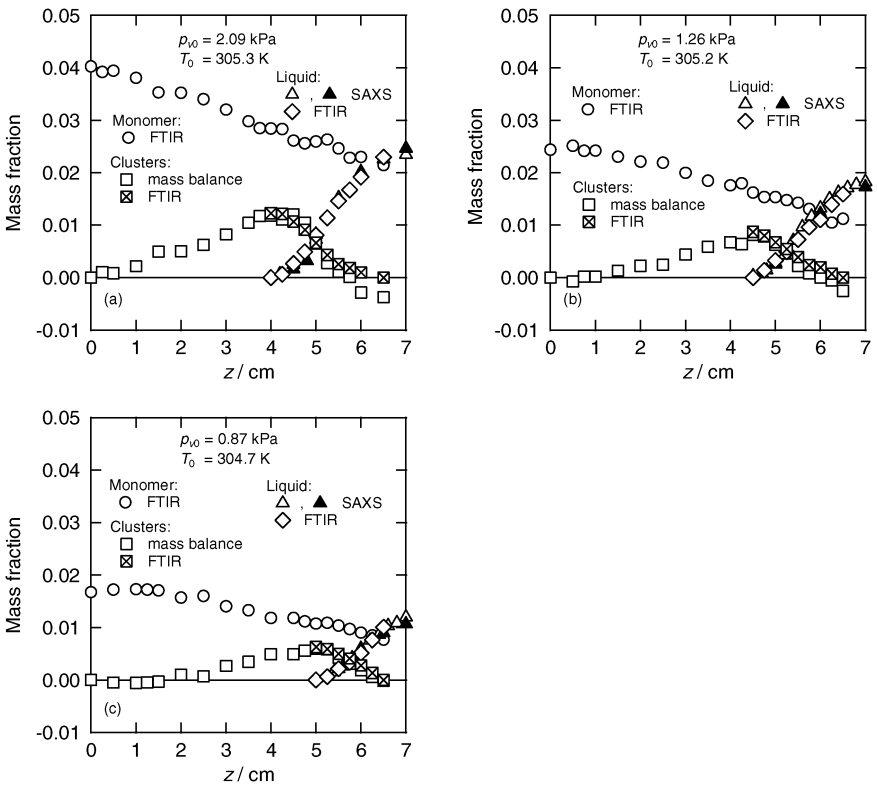

Fig. 10 The methanol cluster and liquid mass fractions determined by fitting the FTIR spectra as described in the text are compared to the values determined by mass balance (clusters) or direct SAXS measurements (liquid) for p_{v0} = (a) 2.09, (b) 1.26, and (c) 0.87 kPa.

So far, we have been able to observe liquid MeOH using both SAXS and FTIR, and the clusters using FTIR. The question remains whether we can observe any evidence for clusters in the SAXS experiments. Since we estimated these clusters would have to be distributed in an aerosol of droplets with an average radius less than ~0.45 nm, scattering features related to the clusters are at much higher q_{SAXS} than those of the larger liquid droplet. In addition, because the scattering intensity scales as $\langle r^6 \rangle$, such small clusters scatter only very weakly. Thus, we need only look at SAXS spectra where cluster concentrations, or number densities, are as high as possible. In our experiments, the highest clusters concentrations correspond to p_{v0} = 2.09 kPa and z = 4.2 cm, just prior to liquid droplet formation. Fig. 11(a) illustrates two SAXS spectra, measured at a nominal SDD of 0.7 m to increase the q_{SAXS} range. The lower spectrum corresponds to the case where the cluster mass fraction equals 1.2×10^{-2}, and is very close to the maximum value observed under any experimental conditions. The upper spectrum corresponds to the same p_{v0} but was measured at z = 7 cm where clusters have been depleted. Although our SAXS experiment setup is not optimized to observe these clusters, the intensity decrease with q_{SAXS} when $q_{SAXS} > 3$ nm^{-1} that is observed in the spectrum measured at z = 4.2 cm is consistent with scattering from small clusters. In contrast, at z = 7 cm, the intensity in the same q_{SAXS} range remains constant suggesting that the scattering is the background scattering from gas molecules rather than that from small clusters. If we fit the scattering expected from a bimodal Schultz distribution of polydisperse spheres to the spectrum at z = 4.2 cm, shown in Fig. 11(a), the average radii for clusters and droplets are 0.45 and 4.5 nm, respectively. Alternatively, on average the clusters contain 6 molecules while the droplets contain ~6000 molecules. The number density of the clusters and droplets are 8.6×10^{15} and 2.3×10^{11} cm^{-3}, respectively. The shape of this bimodal Schultz distribution, plotted as normalized number density against size, is shown in Fig. 11(b). It is qualitatively different from the normalized number distribution found by fitting the spectrum at z = 7 cm, also plotted in Fig. 11(b), which shows the presence of only large droplets. Thus, although our SAXS setup is not optimized to observe these small clusters, these preliminary measurements suggest that on average the clusters contain 6 molecules. These results also suggest that by improving the background scattering and moving to higher q_{SAXS}, SAXS measurements should be able to better characterize cluster size distributions under these experimental conditions. An average cluster size of 6 molecules is also consistent with the heat release observed in Fig. 8(d) since hexamers should have a dissociation enthalpy higher than the tetramer, but lower than the heat of vaporization of the bulk.

IV. Summary and conclusion

We combined PTM, TDLAS, SAXS, and FTIR experiments to study the influence of vapor association on methanol condensation from a dilute vapor–carrier gas mixture in a supersonic nozzle. When the gas mixture is rapidly expanded in the nozzle under our experimental conditions, we observe that up to 30% of the monomer forms clusters prior to the appearance of the liquid. This behavior, driven by methanol's strong association in the vapor phase, is very different from that observed for more normal molecules, such as water. The heat release due to clusters and liquid formation can be observed in PTM and TDLAS temperature measurements. We interpret the gentle deviations in pressure ratio and temperature profiles from the expected isentropic values as cluster formation, and the larger deviations further downstream as liquid droplet formation and growth. With FTIR measurements, we observe that the monomer is continuously consumed as clusters and liquid droplets form. Cluster formation is confirmed by the

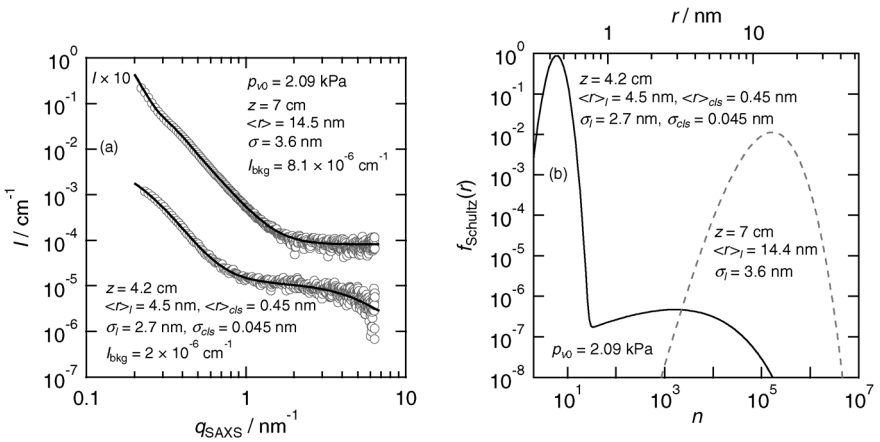

Fig. 11 (a) SAXS spectra at z = 4.2 cm and z = 7 cm for p_{v0} = 2.09 kPa measured at a nominal sample to detector distance (SDD) of 0.7 m. The spectrum at z = 4.2 cm is on the absolute intensity scale while the spectrum at z = 7 cm is offset by a factor of 10 for clarity. The constant intensity with q_{SAXS} when $q_{SAXS} > 3$ nm^{-1} for the spectrum at z = 7 cm suggests there is no scattering from small clusters; while the intensity decrease over the same q_{SAXS} range for the spectrum at z = 4.2 cm suggests scattering from small clusters. In the latter case, the data are well fit by a bimodal size distribution with an average radius of 0.45 nm for the clusters, and an average radius of 4.5 nm for the droplets. (b) The fractional particle size distributions $f_{Schultz}(r)$ derived by fitting the SAXS spectrum at z = 4.2 cm and p_{v0} = 2.09 kPa to scattering from a bimodal Schultz distribution of polydisperse spheres (solid line) and fitting the SAXS spectrum at z = 7 cm and p_{v0} = 2.09 kPa to scattering from a unimodal Schultz distribution of polydisperse spheres (dashed line). The minimum value of n in this figure is 2.

FTIR experiments where we observe the absorption spectra in the OH stretch region that are distinctly different from the monomer and liquid spectra. We observe liquid formation and growth in SAXS experiments and confirm the appearance and increase of the liquid phase by FTIR experiments. In addition, although the monomer–dimer–tetramer equilibrium model predicts the observed monomer depletion, the model cannot match the significant heat release observed during cluster formation, and, thus, predicts the appearance of liquid much earlier than is observed in either the SAXS or the FTIR experiments.

Finally, our experimental results suggest that the process of methanol condensation can be divided into three stages. In the first stage monomer is depleted as small clusters appear, and both the distribution and concentration of these clusters change. In the second stage, clusters continue to be formed but experimental observations cannot definitively establish if the average cluster size is constant or if it continues to increase. In the final stage, liquid droplets start to form *via* nucleation and grow rapidly depleting the monomer and the clusters. The experimental evidence suggests that the clusters present in the second stage are on average larger than the tetramer but smaller than the critical cluster size estimated to be $\sim$24 molecules by classical nucleation theory. The average heat of dissociation of the clusters Δh_{avg} is equal to $\sim$1175 J g^{-1} MeOH. Although our SAXS experiments are not optimized to observe these clusters, preliminary experiments under conditions expected to maximize cluster concentrations, suggest they contain $\sim$6 molecules on average.

Appendix: The adiabatic flow equations for flow with vapor association and condensation in a supersonic nozzle

To account for vapor association in the nozzle, we modify our standard one-dimensional flow equations[34,35] to estimate clusters concentrations and its heat release using an equilibrium model. The final four equations that describe the one-dimensional adiabatic flow with clusters and liquid formation in our supersonic nozzle are

$$\rho = \frac{\rho^* u^*}{u} \Big/ \left(\frac{A}{A^*}\right), \tag{A1}$$

$$\mathrm{d}u = -\frac{\mathrm{d}p}{\rho^* u^*}\left(\frac{A}{A^*}\right), \tag{A2}$$

$$h + \frac{u^2}{2} = h_0, \tag{A3}$$

$$p = \left(\frac{1}{\mu_{avg}}\right)\rho RT, \tag{A4}$$

where ρ, u, p, T, and A are mass density, velocity, static pressure, temperature, and effective flow area respectively. R is the molar gas constant, μ_{avg} is the average molecular weight of the gas mixture, h is the enthalpy per unit mass of gas mixture. The asterisk and subscript 0 denote the value of the variables at the throat and at the stagnation condition respectively.

In eqn (A4), μ_{avg} is calculated by

$$\frac{1}{\mu_{avg}} = \frac{g_{inert}}{\mu_{inert}} + \frac{g_{mono}}{\mu_{mono}} + \sum_n \frac{g_{cls-n}}{\mu_{cls-n}} + \frac{g_l}{\langle \mu_l \rangle}, \tag{A5}$$

where g and μ represent mass fraction and molecular weight respectively. The subscript inert, mono, cls-n, and l denote the inert carrier gas, the methanol monomer, the methanol clusters containing n monomer, and the liquid droplets respectively. The last term $g_l/\langle \mu_l \rangle$ can be neglected in general because the average molecular weight $\langle \mu_l \rangle$ of the droplets is large.

The enthalpy h of the condensing flow is expressed by

$$h = h_0 + \int_{T_0}^{T} c_p^0 \mathrm{d}T - q, \tag{A6}$$

where q is the heat released to the gas mixture by cluster and/or liquid droplet formation, per unit mass of the system, *i.e.* q is the heat of dissociation of the clusters and/or the liquid droplets. c_p^0 is the isobaric heat capacity per unit mass of gas mixture in the fictitious state where clusters and condensation are absent, and can be calculated by

$$c_p^0 = g_{inert} c_{p\text{-inert}} + g_\infty c^0_{p\text{-MeOH(v)}}. \tag{A7}$$

Here $c_{p\text{-inert}}$ is the isobaric heat capacity per unit mass of the carrier gas, and $c^0_{p\text{-MeOH(v)}}$ is the methanol vapor heat capacity in the ideal gas state. The total methanol mass fraction $g_\infty = g_{mono} + \sum_n g_{cls\text{-}n} + g_l$ and g_{inert} are constant in the nozzle. The heat released to the gas mixture by cluster and/or liquid droplet formation q in eqn (A6) is given by

$$q = \sum_n g_{cls\text{-}n} \Delta H_{cls\text{-}n}/\mu_{cls\text{-}n} + g_l \Delta H_{vap}/\mu_l, \tag{A8}$$

where $\Delta H_{cls\text{-}n}$, ΔH_{vap}, and $\mu_l (= \mu_{mono})$ are the molar heat of dissociation of clusters of size n, the molar heat of vaporization of methanol liquid, and molecular weight of methanol, respectively.

In this study, we assume that the clusters and monomers are in equilibrium, and that the equilibrium between clusters of size n (n-mers) and monomers, $A_n \leftrightarrow nA$, can be modeled by

$$p_{cls\text{-}n} = p^n_{mono} \times K_{cls\text{-}n}, \tag{A9}$$

where p_{mono} and $p_{cls\text{-}n}$ are the monomer and n-mer partial pressures, respectively. Here $K_{cls\text{-}n}$ is the formation equilibrium constant that is expressed by

$$K_{cls\text{-}n} = \exp(-\Delta S_{cls\text{-}n}/R + \Delta H_{cls\text{-}n}/RT), \tag{A10}$$

where $\Delta S_{cls\text{-}n}$ and $\Delta H_{cls\text{-}n}$ are the dissociation entropy and enthalpy of size n clusters, respectively.

Finally, the variables p and T are used as input to derive ρ, u, A/A^*, $g_{cls\text{-}n}$ and g_l when we solve eqn (A1)–(A4).

Acknowledgements

This work was supported by the National Science Foundation under Grant number CHE-0911144 and by the Donors of the Petroleum Research Fund administered by the American Chemical Society. Use of the Advanced Photon

Source was supported by the U.S. Department of Energy, Office of Science, Office of Basic Energy Sciences, under Contract No. DE AC02 06CH11357. H.C.A. acknowledges support from NSF CHE-0749807. We thank D. Ghosh, A. Manka, D. Bergmann, J. Wölk, K. Mullick, S. Seifert, and R. Winans for help conducting the SAXS experiments. We thank U. Dieregsweiler for conducting the initial pressure trace measurements that motivated this more detailed study.

References

1 T. De Vries and B. T. Collins, *J. Am. Chem. Soc.*, 1941, **63**, 1343.
2 G. C. Sinke and T. De Vries, *J. Am. Chem. Soc.*, 1953, **75**, 1815.
3 W. Weltner, Jr. and K. S. Pitzer, *J. Am. Chem. Soc.*, 1951, **73**, 2606.
4 E. Strömsöe, H. G. Rönne and A. L. Lydersen, *J. Chem. Eng. Data*, 1970, **15**, 286.
5 J. F. Counsell and D. A. Lee, *J. Chem. Thermodyn.*, 1973, **5**, 583.
6 T. A. Renner, G. H. Kucera and M. Blander, *J. Chem. Phys.*, 1977, **66**, 177.
7 D. J. Frurip, L. A. Curtiss and M. Blander, *Int. J. Thermophys.*, 1981, **2**, 115.
8 L. A. Curtiss, D. J. Frurip and M. Blander, *J. Phys. Chem.*, 1982, **86**, 1120.
9 L. A. Curtiss and M. Blander, *Chem. Rev.*, 1988, **88**, 827.
10 R. J. B. Craven, K. M. De Reuck and W. A. Wakeham, *Pure Appl. Chem.*, 1989, **61**, 1379.
11 E. E. Tucker, S. B. Farnham and S. D. Christian, *J. Phys. Chem.*, 1969, **73**, 3820.
12 R. A. Provencal, J. B. Paul, K. Roth, C. Chapo, R. N. Casaes, R. J. Saykally, G. S. Tschumper and H. F. Schaefer III, *J. Chem. Phys.*, 1999, **110**, 4258.
13 T. Häber, U. Schmitt and M. A. Suhm, *Phys. Chem. Chem. Phys.*, 1999, **1**, 5573.
14 U. Buck and I. Ettischer, *J. Chem. Phys.*, 1998, **108**, 33.
15 U. Buck and F. Huisken, *Chem. Rev.*, 2000, **100**, 3863.
16 C. Steinbach, M. Fárník, I. Ettischer, J. Siebers and U. Buck, *Phys. Chem. Chem. Phys.*, 2006, **8**, 2752.
17 F. Huisken and M. Stemmler, *Z. Phys. D: At., Mol. Clusters*, 1992, **24**, 277.
18 F. Huisken, A. Kulcke, C. Laush and J. M. Lisy, *J. Chem. Phys.*, 1991, **95**, 3924.
19 P. Zielke and M. A. Suhm, *Phys. Chem. Chem. Phys.*, 2006, **8**, 2826.
20 R. W. Larsen, P. Zielke and M. A. Suhm, *J. Chem. Phys.*, 2007, **126**, 194307.
21 H. Bergersen, M. Abu-samha, A. Lindblad, R. R. T. Marinho, G. Öhrwall, M. Tchaplyguine, K. J. Børve, S. Svensson and O. Björneholm, *J. Chem. Phys.*, 2006, **125**, 184303.
22 F. C. Hagemeister, C. J. Gruenloh and T. S. Zwier, *J. Phys. Chem. A*, 1998, **102**, 82.
23 S. L. Boyd and R. J. Boyd, *J. Chem. Theory Comput.*, 2007, **3**, 54.
24 M. M. Pires and V. F. DeTuri, *J. Chem. Theory Comput.*, 2007, **3**, 1073.
25 M. S. El-Shall, D. Wright, Y. Ibrahim and H. Mahmoud, *J. Phys. Chem. A*, 2003, **107**, 5933.
26 D. Wright and M. S. El-Shall, *J. Chem. Phys.*, 1996, **105**, 11199.
27 M. Falk and E. Whalley, *J. Chem. Phys.*, 1961, **34**, 1554.
28 K. Ohno, T. Shimoaka, N. Akai and Y. Katsumoto, *J. Phys. Chem.A*, 2008, **112**, 7342.
29 Y. J. Kim, B. E. Wyslouzil, G. Wilemski, J. Wölk and R. Strey, *J. Phys. Chem. A*, 2004, **108**, 4365.
30 D. Ghosh, A. Manka, R. Strey, S. Seifert, R. E. Winans and B. E. Wyslouzil, *J. Chem. Phys.*, 2008, **129**, 124302.
31 D. Ghosh, D. Bergmann, R. Schwering, J. Wölk, R. Strey, S. Tanimura and B. E. Wyslouzil, *J. Chem. Phys.*, 2010, **132**, 024307.
32 R. Strey, T. Schmeling and P. E. Wagner, *J. Chem. Phys.*, 1986, **85**, 6192.
33 F. Peters and B. Paikert, *J. Chem. Phys.*, 1989, **91**, 5672.
34 B. E. Wyslouzil, C. H. Heath, J. L. Cheung and G. Wilemski, *J. Chem. Phys.*, 2000, **113**, 7317.
35 S. Tanimura, Y. Zvinevich, B. E. Wyslouzil, M. S. Zahniser, J. H. Shorter, D. D. Nelson and J. B. McManus, *J. Chem. Phys.*, 2005, **122**, 194304.
36 S. Tanimura, B. E. Wyslouzil and G. Wilemski, *J. Chem. Phys.*, 2010, **132**, 144301.
37 P. Paci, Y. Zvinevich, S. Tanimura, B. E. Wyslouzil, M. Zahniser, J. Shorter, D. Nelson and B. McManus, *J. Chem. Phys.*, 2004, **121**, 9964.
38 S. Tanimura, B. E. Wyslouzil, M. S. Zahniser, J. H. Shorter, D. D. Nelson and J. B. McManus, *J. Chem. Phys.*, 2007, **127**, 034305.
39 B. E. Wyslouzil, G. Wilemski, R. Strey, S. Seifert and R. E. Winans, *Phys. Chem. Chem. Phys.*, 2007, **9**, 5353.
40 http://www.aerodyne.com/.
41 L. S. Rothman, D. Jacquemart, A. Barbe, D. C. Benner, M. Birk, L. R. Brown, M. R. Carleer, C. Chackerian Jr., K. Chance, L. H. Coudert, V. Dana, V. M. Devi, J.-M. Flaud, R. R. Gamache, A. Goldman, J.-M. Hartmann, K. W. Jucks, A. G. Maki, J.-Y. Mandin, S. T. Massie, J. Orphal, A. Perrin, C. P. Rinsland, M. A. H. Smith, J. Tennyson, R. N. Tolchenov, R. A. Toth, J. Vander Auwera, P. Varanasi and G. Wagner, *J. Quant. Spectrosc. Radiat. Transfer*, 2005, **96**, 139.
42 S. Seifert, R. E. Winans, D. M. Tiede and P. Thiyagarajan, *J. Appl. Crystallogr.*, 2000, **33**, 782.
43 T. C. Huang, H. Toraya, T. N. Blanton and Y. Wu, *J. Appl. Crystallogr.*, 1993, **26**, 180.
44 T. N. Blanton, T. C. Huang, H. Toraya, C. R. Hubbard, S. B. Robie, D. Louer, H. E. Göbel, R. Gilles and T. Raferty, *Powder Diffr.*, 1995, **10**, 91.
45 M. Megens, C. M. van Katz, P. Bösecke and W. L. Vos, *Langmuir*, 1997, **13**, 6120.
46 M. Kotlarchyk and S. H. Chen, *J. Chem. Phys.*, 1983, **79**, 2461.
47 *Lange's Handbook of Chemistry*, ed. J. A. Dean, McGraw-Hill, New York, 14th edn, 1992.
48 R. D. Goodwin, *J. Phys. Chem. Ref. Data*, 1987, **16**, 799.
49 T. Schmeling and R. Strey, *Ber. Bunsen–Ges. Phys. Chem.*, 1983, **87**, 871.
50 R. S. McDowell and F. H. Cruse, *J. Chem. Eng. Data*, 1963, **8**, 547.
51 To calculate the centerline temperature in Fig. 3 we included the effects of clustering and used the equilibrium constants from ref. 3. We note, however, that the calculated centerline temperatures vary by less than 0.02 K whether we include or ignore the cluster formation process.
52 A. Obeidat, M. Gharaibeh, H. Ghanem, F. Hrahsheh, N. Al-Zoubi and G. Wilemski, *ChemPhysChem*, 2010, **11**, 3987.
53 H. Laksmono, S. Tanimura and B. E. Wyslouzil, manuscript in preparation.
54 R. Strey, P. E. Wagner and T. Schmeling, *J. Chem. Phys.*, 1986, **84**, 2325.
55 C. Cézard, C. A. Rice and M. A. Suhm, *J. Phys. Chem. A*, 2006, **110**, 9839.
56 M. Paolantoni, P. Sassi, A. Morresi and R. S. Cataliotti, *Chem. Phys.*, 2005, **310**, 169.
57 H. Laksmono, *Experimental Study of Methanol Condensation and Nucleation in Supersonic Nozzles*, Ph.D. Thesis, The Ohio State University, 2010.